Aerospace Science and Technology 114 (2021) 106742

Contents lists available at ScienceDirect

Aerospace Science and Technology

www.elsevier.com/locate/aescte

A bi-bandwidth extended state observer for a system with measurement noise and its application to aircraft with abrupt structural damage

Lingyu Yang [a], Lilei Liu [a,b], Jing Zhang [a,*]

[a] School of Automation Science and Electrical Engineering, Beihang University, Beijing, 100191, China
[b] Expace Technology Co, Ltd., Wuhan Hubei, 430000, China

ARTICLE INFO

Article history:
Received 4 November 2020
Received in revised form 21 February 2021
Accepted 12 April 2021
Available online 26 April 2021
Communicated by Jayaram Sanjay

Keywords:
Extended state observer
Multisource uncertainty
Measurement noise
Flight control

ABSTRACT

In this paper, we address the problem of disturbance estimation for a class of linear systems with both fast time-varying uncertainty and measurement noise. A novel bi-bandwidth extended state observer (BESO) is proposed to achieve fast disturbance tracking and satisfactory noise suppression. The direction information of the estimation errors is used through a directional switching operator (DSO) to dynamically tune the bandwidth of the BESO. Sufficient conditions for the stability of the BESO are given, and the error dynamics are proven to be bounded and to converge in finite time. A comprehensive comparison of the BESO and three other representative approaches is presented, which shows that the BESO achieves a performance improvement of greater than 13%. A closed-loop control application for a structurally damaged aircraft is also provided to demonstrate the effectiveness and efficiency of the BESO.

1. Introduction

Inaccuracies inevitably exist between an actual system and a mathematical model of the system, and the system therefore deviates from the expected characteristics. In practice, uncertainties are usually multisource and time varying and may sometimes jump, for example, a strong gust striking a spacecraft [1], abrupt structural damage in flight [2] and failure of some critical equipment [3]. Such jump disturbances usually cause control surface saturation and are of extreme harm to system safety. Additionally, the magnitude of uncertainties and their derivatives continuously change with the system state or time. Therefore, estimating these uncertainties precisely without much conservation has been a great challenge in the control of disturbed systems.

In this paper, we pay particular attention to extended state observers (ESOs), which lump model uncertainties and disturbances into a total disturbance without discrimination and have promising speed and robustness compared to disturbance observers [4–7], reduced-order disturbance observers [8], nonlinear disturbance observers [9,10], sliding mode disturbance observers [11,12], unknown input observers [13,14] and other similar approaches [15]. ESOs have attracted wide and long-lasting attention from theoretical researchers, and overviews of early developments are presented in [16–18]. Gao [19] has performed prospective work on stability proofs and parameter selection for the linear extended state observer (LESO). Zhao [20,21] has made significant breakthroughs in recent works on stability proofs for the nonlinear extended state observer (NESO). ESOs have also shown great advantages in many industrial applications, such as aeronautics [22,23,2], fault-tolerant control [24–26] and other scenarios [27–30].

An important feature of an ESO is that its estimation performance can be improved arbitrarily as the bandwidth or gain increases, regardless of whether it is in a steady-state phase or transient phase or whether the disturbance is strong. However, the result may not hold consistently in the presence of measurement noise, which is indeed omnipresent in actual scenarios [31–34]. An inevitable contradiction exists between measurement noise sensitivity and state reconstruction speed [31], and the reconstructed state oscillates intensely under high gain conditions when measurement noise exists [32,33]. Additionally, a high-order and large-bandwidth observer may amplify the measurement noise to an unacceptable level and thereby impact the closed-loop system performance [34,14]. This analysis shows that the high-gain or bandwidth approach may fail in the presence of noise, and we need to pay particular attention to compromises between measurement noise attenuation and transient process speed.

Considerable effort has been made to strike a balance between state estimation error attenuation and transient process speed. Wang [35] proposed a time-varying ESO that estimates a

* Corresponding author.
E-mail address: zhangjing2013@buaa.edu.cn (J. Zhang).

https://doi.org/10.1016/j.ast.2021.106742
1270-9638/

nonuniform bounded disturbance. Pu [36] designed a linear time-varying ESO that combines both the advantages of the theoretical completeness of the LESO and the good practical performance of the NESO. Li [37] implemented linear–nonlinear switching in an LESO and an NESO to cope with scenarios with different disturbance levels. However, sufficient results when noise exists are still lacking, and this remains an open issue. Han proposed a filter-based approach in his monograph; the approach requires noise-contaminated measurements to be preprocessed via a filter before they are input into the ESO, but notable lagging exists in his simulations [38]. Dong [39] introduced a perturbation constant into an ESO and showed that the perturbation constant can alter the sensitivity of the system to noise. However, this method does not provide an effective online adjustment approach for the perturbation constant. Zhang [40] proposed an offline gain optimization method for a nonlinear third-order ESO to suppress measurement noise. Won [41] introduced auxiliary state variables to avoid amplification of the measurement noise in a high-gain disturbance observer. Xue proposed the adaptive extended state observer (AESO) approach, which adopts an adaptive Kalman filter-like gain law, and implemented it in a gasoline engine cylinder pressure control task [42]. The boundary of the disturbance derivative is adopted as prior information for the AESO; however, an appropriate boundary is usually difficult to determine in the case of multisource disturbance, especially in the case of abruptly changing disturbance. Prasov proposed a novel nonlinear high-gain observer (NHGO) that implements a gain scheduling strategy contradictory to the NESO approach; i.e., it uses a high gain for large errors and a low gain for small ones [43,44]. Cheng [45] adopted a similar approach and proposed an ESO that switches between two gain values; however, the switch boundary must be carefully tuned based on the bounded noise, and an inappropriate boundary may lead to significant performance degradation.

Because the disturbance in an actual system is always multisource and time varying, a predefined boundary may lead the observer to be either too conservative or too fragile. An ESO that has both speed from high gain and denoising capability from low gain can help eliminate this problem. Therefore, we propose a novel bi-bandwidth extended state observer (BESO), and the error deviation direction is introduced to the proposed BESO to achieve a good compromise between transient process speed and steady-state noise attenuation. In addition, the approach makes no strong assumptions about disturbance and measurement noise, similar to the LESO, which alleviates the conservativeness that may exist in the AESO or the nonlinear high-gain ESO (NHGESO).

There are four main contributions of this work.

1) A novel BESO approach is proposed, and a directional switching operator (DSO) and bi-bandwidth scaling factor (BSF) are introduced to address the disturbance estimation problem for systems with measurement noise and multisource uncertainties.

2) Sufficient conditions, i.e., feasible regions of the BSF, for the stability of a general second-order BESO and a bandwidth-based second-order BESO are given. In addition, the estimation error is proven to be bounded and to converge in finite time.

3) The BESO is applicable in whole-state measurable multiple-input multiple-output (MIMO) systems.

4) Detailed comparisons between the BESO and three promising ESO approaches are presented, and a closed-loop control application for a structurally damaged aircraft is provided to demonstrate the effectiveness and efficiency of the BESO.

The main structure of this article is as follows: In section 2, the detailed mathematical descriptions of the problem are formulated. A rigorous proof of the stability of the BESO is given in section 3, followed by a numerical simulation comparison in section 4 and an application case of fault-tolerant flight control for a structurally damaged aircraft in section 5. Finally, conclusions and future plans are described.

2. Problem formulation

A MIMO system with parameter uncertainty, disturbance and measurement noise can be formulated as shown in (1) and (2).

$$\dot{\boldsymbol{x}} = \boldsymbol{A}\boldsymbol{x} + \boldsymbol{B}\boldsymbol{u} + \underbrace{(\Delta\boldsymbol{A}\boldsymbol{x} + \Delta\boldsymbol{B}\boldsymbol{u} + \boldsymbol{d})}_{\boldsymbol{f}}, \tag{1}$$

$$\boldsymbol{x}_m = \boldsymbol{x} + \boldsymbol{n}_{\boldsymbol{x}}, \tag{2}$$

where $\boldsymbol{x} \in \mathbb{R}^n$ is the state vector, $\boldsymbol{u} \in \mathbb{R}^m$ is the input, and $\boldsymbol{A}$ and $\boldsymbol{B}$ are matrices with proper dimensions. The model uncertainties are denoted as $\Delta\boldsymbol{A}$ and $\Delta\boldsymbol{B}$, while the disturbance is referred to as $\boldsymbol{d} \in \mathbb{R}^n$, and $(\Delta\boldsymbol{A}\boldsymbol{x} + \Delta\boldsymbol{B}\boldsymbol{u} + \boldsymbol{d})$ represents the so-called total disturbance $\boldsymbol{f}(\boldsymbol{x}, \boldsymbol{u}, \boldsymbol{d}) : \mathbb{R}^n \times \mathbb{R}^m \times \mathbb{R}^m \mapsto \mathbb{R}^n$.

In general, $\boldsymbol{f}$ and its derivatives are assumed to have known upper bounds; however, appropriate bounds are usually difficult to determine in practice. As shown in (1), $\boldsymbol{f}$ contains multiple components, among which the external disturbance $\boldsymbol{d}$ can be time-varying; $\Delta\boldsymbol{A}$ and $\Delta\boldsymbol{B}$ may be constant, slowly time-varying or switching functions when abrupt failure occurs; $\boldsymbol{x}$ is usually considered a relatively fast time-varying parameter but may not be bounded unless the system is stable or can be stabilized by the controller; and $\boldsymbol{u}$ is also quickly time-varying and may be a step signal—i.e., $\mathrm{d}\boldsymbol{u}/\mathrm{d}t$ is infinite. Therefore, $\boldsymbol{f}$ is a complex and multisource disturbance, and using a unified boundary may lead the observer to be conservative or cause high gain problems.

In this paper, we represent $\boldsymbol{f}$ as a combination of two parts, a continuous time-varying component $\boldsymbol{f}_a$ and a switching component $\boldsymbol{f}_b$, as shown below.

$$\boldsymbol{f} = \boldsymbol{f}_a + \boldsymbol{f}_b. \tag{3}$$

Note that this paper focuses on the disturbance observation problem. We can assume that either system (1) is stable or the closed loop is stable; i.e., $\boldsymbol{x}$ is bounded. Therefore, $\boldsymbol{f}_a$ and its derivative are also bounded as

$$\|\boldsymbol{f}_a\|_2 \le m_a, \ \|\dot{\boldsymbol{f}}_a\|_2 \le \omega_a. \tag{4}$$

$\boldsymbol{f}_b$ stands for abrupt interference, which may be caused by system failure or due to a step control input, and can be expressed as a sum of a series of impulse functions:

$$\dot{\boldsymbol{f}}_b = \sum_{i}^{l_b} \boldsymbol{b}_i \delta(t - t_i), \tag{5}$$

where $\boldsymbol{b}_i$ is the disturbance increment at time t_i, $\boldsymbol{f}_b$ is assumed to be bounded as $\|\boldsymbol{f}_b\|_2 \le m_b$, $\delta(\tau)$ represents the unit impulse function, and the impulse series is assumed to be sparse, i.e.,

$$\sup_i (t_{i+1} - t_i) \ge T, \tag{6}$$

where T represents the upper bound of the estimator transition time.

Eq. (2) illustrates that the state $\boldsymbol{x}$ can be measured but is mixed with noise $\boldsymbol{n}_{\boldsymbol{x}}$, where the actual measurement is $\boldsymbol{x}_m$. $\boldsymbol{n}_{\boldsymbol{x}}$ is high-frequency noise, which is assumed to be restricted as

$$\|\boldsymbol{n}_{\boldsymbol{x}}\| = m_c \ll \min(m_a, m_b). \tag{7}$$

The goal of this paper is to estimate the state $\boldsymbol{x}$ and the total disturbance $\boldsymbol{f}$ in system (1) with an acceptable steady-state error and acceptable transient properties when measurement noise $\boldsymbol{n}_{\boldsymbol{x}}$ exists.

3. The bi-bandwidth extended state observer

In this section, the novel BESO is proposed. First, the BESO for a single-input single-output (SISO) system with measurement noise is given.

3.1. BESO for a SISO system

The SISO case for systems (1) and (2) can be described as

$$\dot{x} = ax + bu + f, \tag{8}$$

$$x_m = x + n_x. \tag{9}$$

The general form of a BESO for the above SISO system is given as

$$\begin{cases} e_m = \hat{x} - x_m \\ \gamma = \eta^{-\text{sign}(\text{d}|e_m|/\text{dt})} \\ \dot{\hat{x}} = ax_m + bu + \hat{f} + \beta_1 \gamma e_m \\ \dot{\hat{f}} = \beta_2 \gamma^2 e_m \end{cases}, \tag{10}$$

where e_m is the estimation error relative to the state measurement and β_1 and β_2 are the gains of the observer. In particular, when β_1 and β_2 are chosen through a bandwidth approach, as in (11), the system is called a bandwidth-based BESO.

$$\beta_1 = -2\omega_o,\ \beta_2 = -\omega_o^2, \tag{11}$$

where $\omega_o > 0$ is defined as the base bandwidth of the BESO.

Comparing (10) with standard ESOs, the bandwidth of the BESO is not related only to β_i but is also affected by a new term γ. γ is defined as the directional switching operator (DSO) of the BESO, and η is defined as the corresponding bi-bandwidth scaling factor (BSF). Because of the introduction of γ and η, the proposed BESO approach has some unique properties:

1) The DSO introduces additional information to ESO, i.e., the direction of the absolute value of the estimated error rate. Consequently, the proposed BSEO has more freedom and may be more efficient than a traditional ESO.

2) When η is chosen to be 1, the BESO is equivalent to a traditional LESO. Therefore, this BESO is actually an extension of traditional ESOs.

3) In the case of $\eta_i \neq 1$, the proposed BESO has a so-called bi-bandwidth property: when the estimation error is directed toward the origin, the bandwidth or the observer gain will be multiplied by η; otherwise, they will be divided by η. In particular, for a system with measurement noise, a BESO with $\eta < 1$ outperforms one with $\eta > 1$.

4) There are only two degrees of freedom of the adjustable parameters of the bandwidth-based BESO, i.e., the base bandwidth and the BSF, which means the tuning process is relatively simple.

5) Compared to obtaining the value of the differential of e_m, it is easier and more accurate to obtain its sign. Therefore, the calculation of the DSO will not affect the practicality of the proposed BESO.

Based on the above factors, BESO represents a synthesis of two LESOs with different bandwidths. Moreover, although each LESO is linear, the switching mechanism, i.e., the DSO, makes the BESO a nonlinear observer that, thus, potentially has fast tracking and noise suppression capabilities.

Theorem 1. *The sufficient conditions for the BESO in (10) to be stable are as follows:*

1) $\beta_i < 0$ $(i = 1, 2)$, *and*

2) $\eta^2 + 1/\eta^2 - 2 < -\beta_1^2/\beta_2$.

Proof. By subtracting (8) from (10) and letting $e_x = \hat{x} - x$ and $e_f = \hat{f} - f$, the error dynamics are formulated as

$$\begin{cases} \dot{e}_x = \beta_1 \gamma e_x + e_f + (a - \beta_1 \gamma) n_x \\ \dot{e}_f = \beta_2 \gamma^2 e_x - (\dot{f}_a + \dot{f}_b + \beta_2 \gamma^2 n_x) \end{cases}. \tag{12}$$

(12) can be rewritten as

$$\begin{bmatrix} \dot{e}_x \\ \dot{e}_f \end{bmatrix} = \boldsymbol{A}_\gamma \begin{bmatrix} e_x \\ e_f \end{bmatrix} + \boldsymbol{h}, \tag{13}$$

where

$$\boldsymbol{A}_\gamma = \begin{bmatrix} \beta_1 \gamma & 1 \\ \beta_2 \gamma^2 & 0 \end{bmatrix},\ \boldsymbol{h} = \begin{bmatrix} (a - \beta_1 \gamma) n_x \\ -\dot{f}_a - \dot{f}_b - \beta_2 \gamma^2 n_x \end{bmatrix}. \tag{14}$$

Although $\beta_1 < 0$ and $\beta_2 < 0$ make $\boldsymbol{A}_\gamma$ a Hurwitz matrix, this cannot guarantee the stability of the system since γ may switch between η and $1/\eta$. Therefore, we need to find a positive–definite real symmetric matrix $\boldsymbol{P}$ that simultaneously satisfies the matrix inequalities

$$\begin{aligned} \boldsymbol{A}_{\bar{\gamma}}^\top \boldsymbol{P} + \boldsymbol{P} \boldsymbol{A}_{\bar{\gamma}} &\leq -2\mu \boldsymbol{I}, \\ \boldsymbol{A}_{\underline{\gamma}}^\top \boldsymbol{P} + \boldsymbol{P} \boldsymbol{A}_{\underline{\gamma}} &\leq -2\mu \boldsymbol{I}, \end{aligned} \tag{15}$$

where $\mu > 0$ and

$$\boldsymbol{A}_{\bar{\gamma}} = \begin{bmatrix} \beta_1/\eta & 1 \\ \beta_2/\eta^2 & 0 \end{bmatrix},\ \boldsymbol{A}_{\underline{\gamma}} = \begin{bmatrix} \beta_1 \eta & 1 \\ \beta_2 \eta^2 & 0 \end{bmatrix}. \tag{16}$$

The existence of $\boldsymbol{P}$, or the so-called common quadratic Lyapunov function (CQLF) for two arbitrary systems, is usually difficult to prove [46]. Fortunately, $\boldsymbol{A}_{\bar{\gamma}}$ and $\boldsymbol{A}_{\underline{\gamma}}$ yield the following condition:

$$\text{rank}(\boldsymbol{A}_{\bar{\gamma}} - \boldsymbol{A}_{\underline{\gamma}}) = \text{rank}\left(\begin{bmatrix} \beta_1/\eta - \beta_1 \eta & 0 \\ \beta_2/\eta^2 - \beta_2 \eta^2 & 0 \end{bmatrix} \right) = 1. \tag{17}$$

Therefore, the existence of the CQLF of the above switched system can be simplified as 1) both $\boldsymbol{A}_{\bar{\gamma}}$ and $\boldsymbol{A}_{\underline{\gamma}}$ are Hurwitz, and 2) the matrix product $\boldsymbol{A}_{\bar{\gamma}} \boldsymbol{A}_{\underline{\gamma}}$ does not have any eigenvalues on the negative part of the real axis [46,47]. According to (16), we have

$$\text{eig}(\boldsymbol{A}_{\bar{\gamma}} \boldsymbol{A}_{\underline{\gamma}}) = 0.5(\sigma \pm \sqrt{\sigma^2 - 4\beta_2^2}), \tag{18}$$

where $\sigma = \beta_2(\eta^2 + 1/\eta^2) + \beta_1^2$. To ensure that $\boldsymbol{A}_{\bar{\gamma}} \boldsymbol{A}_{\underline{\gamma}}$ has no negative real eigenvalues, the following conditions must be met:

$$\sigma \geq 0 \text{ or } 2\beta_2 < \sigma < 0. \tag{19}$$

Note that $\beta_2 < 0$; consequently, the above conditions can be simplified to $\sigma > 2\beta_2$, i.e., $\beta_2(\eta^2 + 1/\eta^2) + \beta_1^2 > 2\beta_2$. Thus, Theorem 1 is proven. □

Corollary 1. *If* β_1 *and* β_2 *are chosen as in (11) with* $\omega_o > 0$, *the sufficient condition for the bandwidth-based BESO to be stable is* $\sqrt{2} - 1 < \eta < \sqrt{2} + 1$.

Theorem 2. *For a BESO that satisfies Corollary 1, the 2-norm of the estimation error* $\boldsymbol{e} = [e_x, e_f]^\top$ *is bounded, and* $\boldsymbol{e}$ *will exponentially converge to a finite error bound in each jump disturbance interval.*

Proof. Denote $\boldsymbol{\epsilon} = \boldsymbol{W}\boldsymbol{e}$, where $\boldsymbol{W} = \text{diag}(1, \omega_o^{-1})$; (13) can be rewritten as

$$\dot{\boldsymbol{\epsilon}} = \omega_o \boldsymbol{A}'_\gamma \boldsymbol{\epsilon} + \boldsymbol{h}', \tag{20}$$

where

$$\boldsymbol{A}'_{\gamma} = \begin{bmatrix} -2\gamma & 1 \\ -\gamma^2 & 0 \end{bmatrix}, \ \boldsymbol{h}' = \begin{bmatrix} (a+2\omega_o\gamma)n_x \\ -\frac{\dot{f}_a}{\omega_o} + \omega_o\gamma^2 n_x \end{bmatrix}. \tag{21}$$

Since $\boldsymbol{A}'_{\gamma}$ can be regarded as a special form of $\boldsymbol{A}_{\gamma}$ under the condition $\omega_o = 1$, there exists a positive-definite symmetric matrix $\boldsymbol{P}'$ such that

$$\begin{aligned} \boldsymbol{A}'^{\top}_{\bar{\gamma}} \boldsymbol{P}' + \boldsymbol{P}' \boldsymbol{A}'_{\bar{\gamma}} \leq -2\mu \boldsymbol{I} \\ \boldsymbol{A}'^{\top}_{\underline{\gamma}} \boldsymbol{P}' + \boldsymbol{P}' \boldsymbol{A}'_{\underline{\gamma}} \leq -2\mu \boldsymbol{I} \end{aligned}. \tag{22}$$

Note that $\boldsymbol{P}'$ is determined by γ and a predefined scalar μ and is not affected by ω_o.

We can choose a candidate Lyapunov function as $V = \boldsymbol{\epsilon}^{\top} \boldsymbol{P}' \boldsymbol{\epsilon}/2$, and the derivative of V along the trajectory is

$$\begin{aligned} \dot{V} &= \boldsymbol{\epsilon}^{\top} \omega_o (\boldsymbol{A}'^{\top}_{\gamma} \boldsymbol{P}' + \boldsymbol{P}' \boldsymbol{A}'_{\gamma}) \boldsymbol{\epsilon} + \boldsymbol{\epsilon}^{\top} \boldsymbol{P}' \boldsymbol{h}' \\ &\leq -\mu\omega_o ||\boldsymbol{\epsilon}||_2^2 + \lambda_{\max}(\boldsymbol{P}') ||\epsilon||_2 \left|\left|\boldsymbol{h}'\right|\right|_2. \end{aligned} \tag{23}$$

We choose

$$L_1 = 2\lambda^3_{\max}(\boldsymbol{P}') \left(\frac{||\boldsymbol{h}'||_2}{\mu\omega_o} \right)^2. \tag{24}$$

If $V(\boldsymbol{\epsilon}) > L_1$, it follows that

$$\dot{V}(\boldsymbol{\epsilon}) \leq -\frac{\mu\omega_o}{2\lambda_{\max}(\boldsymbol{P}')} V(\boldsymbol{\epsilon}). \tag{25}$$

Therefore, any $\boldsymbol{\epsilon}$ outside the bound $\boldsymbol{U} = \{\boldsymbol{\epsilon} | V(\boldsymbol{\epsilon}) < L_1\}$ will converge to $\boldsymbol{U}$, and the convergence time is less than T, which satisfies

$$T = \frac{2\lambda_{\max}(\boldsymbol{P}')}{\mu\omega_o} \ln \frac{V_0}{L_1}, \tag{26}$$

where V_0 is the initial value of $V(\boldsymbol{\epsilon})$.

Note that L_1 is actually the bound of $\boldsymbol{\epsilon}$; to obtain the bound of $\boldsymbol{e}$, we recall that

$$V(\boldsymbol{\epsilon}) = \boldsymbol{e}^{\top} \boldsymbol{W} \boldsymbol{P}' \boldsymbol{W} \boldsymbol{e} \geq ||\boldsymbol{e}||_2^2 \lambda_{\min}(\boldsymbol{P}')/\omega_o^2. \tag{27}$$

Thus, the following condition needs to hold to guarantee $V(\boldsymbol{\epsilon}) > L_1$:

$$||\boldsymbol{e}||_2^2 > L_2, \tag{28}$$

where

$$\begin{aligned} L_2 &= 2\frac{\lambda^3_{\max}(\boldsymbol{P}')}{\lambda_{\min}(\boldsymbol{P}')} \left(\frac{||\boldsymbol{h}||'_2}{\mu} \right)^2 \\ &= 2\frac{\lambda^3_{\max}(\boldsymbol{P}')}{\mu^2\lambda_{\min}(\boldsymbol{P}')} \left((a+2\omega_o\gamma)^2 n_x^2 + \left(\omega_o\gamma^2 n_x - \frac{\dot{f}_a}{\omega_o} \right)^2 \right), \end{aligned} \tag{29}$$

and we can further assume that f_a and n_x are bounded as (4) and (7). Therefore, (29) can be simplified to

$$\begin{aligned} L_2 \leq L_3 = 2\frac{\lambda^3_{\max}(\boldsymbol{P}')}{\mu^2\lambda_{\min}(\boldsymbol{P}')} \Bigg(&((a+2\omega_o\gamma)^2 + \omega_o^2\gamma^4) m_c^2 \\ &+ 2\gamma^2\omega_a m_c + \left(\frac{\omega_a}{\omega_o} \right)^2 \Bigg). \end{aligned} \tag{30}$$

(30) and (26) directly illustrate Theorem 2. □

Through the above analysis, we show that observer (10) is bounded and is exponentially convergent when no jump is considered. If we can prove that the observer is still bounded in a interval containing a sudden jump, we say the observer is bounded in the whole time domain.

According to (5) and (6), f_b is almost everywhere continuous in the time domain, and the Lebesgue integration of $\dot{f}_b$ exists in a narrow interval with the following form:

$$\int_{t_i^-}^{t_i^+} \dot{f}_b \mathrm{d}t = b_i, \tag{31}$$

where $t_i^- < t_i < t_i^+$. Note that $\dot{f}_b(t_i) = b_i\delta(t_i)$ is a impulse signal with no sign change in $[t_i^-, t_i^+]$, we can write

$$\left| \int_{t_i^-}^{t_i^+} \dot{f}_b \mathrm{d}t \right| = \int_{t_i^-}^{t_i^+} \left| \dot{f}_b \right| \mathrm{d}t = |b_i|. \tag{32}$$

To complete the proof, we start from the Lyapunov function (23):

$$\dot{V} \leq -\mu\omega_o \|\boldsymbol{\epsilon}\|_2^2 + \lambda_{\max}(\boldsymbol{P}') \|\boldsymbol{\epsilon}\|_2 \|\boldsymbol{h}''\|_2, \tag{33}$$

where

$$\begin{aligned} \boldsymbol{h}'' &= \begin{bmatrix} (a+2\omega_o\gamma)n_x \\ -\frac{\dot{f}_a+\dot{f}_b}{\omega_o} + \omega_o\gamma^2 n_x \end{bmatrix} = \begin{bmatrix} (a+2\omega_o\gamma)n_x \\ -\frac{\dot{f}_a}{\omega_o} + \omega_o\gamma^2 n_x \end{bmatrix} + \begin{bmatrix} 0 \\ -\frac{\dot{f}_b}{\omega_o} \end{bmatrix} \\ &= \boldsymbol{h}_1 + \boldsymbol{h}_2. \end{aligned} \tag{34}$$

Considering

$$-\|\boldsymbol{\epsilon}\|_2^2 \leq -\frac{V}{\lambda_{\max}(\boldsymbol{P}')}, \ \|\boldsymbol{\epsilon}\|_2 \leq \sqrt{\frac{V}{\lambda_{\min}(\boldsymbol{P}')}}. \tag{35}$$

(33) can be expanded as

$$\dot{V} \leq -c_1 V + c_2 \sqrt{V} (\|\boldsymbol{h}_1\|_2 + \|\boldsymbol{h}_2\|_2), \tag{36}$$

where $c_1 = \mu\omega_o/\lambda_{\max}(\boldsymbol{P}')$ and $c_2 = \lambda_{\max}(\boldsymbol{P}')/\sqrt{\lambda_{\min}(\boldsymbol{P}')}$.

Divide both sides with $\sqrt{V}$, we get

$$\frac{\dot{V}}{\sqrt{V}} \leq -c_1\sqrt{V} + c_2(\|\boldsymbol{h}_1\|_2 + \|\boldsymbol{h}_2\|_2). \tag{37}$$

Note that

$$\frac{\mathrm{d}\sqrt{V}}{\mathrm{d}t} = \frac{\dot{V}}{\sqrt{V}}, \tag{38}$$

we can rewrite (38) to

$$\dot{v} \leq -c_1 v + c_2(\|\boldsymbol{h}_1\|_2 + \|\boldsymbol{h}_2\|_2), \tag{39}$$

where $v = \sqrt{V}$. (39) is a first-order non-homogeneous linear differential equations, therefore, its root has the following form

$$v(t) \leq e^{-c_1(t-t_0)} v(t_0) + \int_{t_0}^{t} e^{c_1(\tau-t)} c_2(\|\boldsymbol{h}_1\|_2 + \|\boldsymbol{h}_2\|_2) \mathrm{d}\tau. \tag{40}$$

Without loss of generality, we choose $t_0 = t_i^-$ and $t = t_i^+$, recalling that the impulse series $\dot{f}_b$ is assumed to be sparse, namely $v(t_i^-) = M < \infty$, we can write

$$v(t_i^+) \leq M + \int_{t_i^-}^{t_i^+} c_2 \|\boldsymbol{h}_1\|_2 \mathrm{d}\tau + \int_{t_i^-}^{t_i^+} \frac{c_2}{\omega_o} |\dot{f}_b| \mathrm{d}\tau. \tag{41}$$

Combining (32), $\|\boldsymbol{h}_1\|_2 < \infty$ and $t_i^+ - t_i^- \to 0$, we get

$$v(t_i^+) \le M + \frac{c_2}{\omega_o} b_i. \tag{42}$$

Eq. (42) indicates that after a sudden bounded jump, the bound of $\boldsymbol{\epsilon}$ exists. Combined with Theorem 2, we can conclude that the observer (10) is bounded in the whole time domain when a jump disturbance exists.

Remark 1. For the bandwidth-based BESO, its transient process is affected by the base bandwidth, and a greater ω_o means faster convergence. In addition, the actual transient time is also affected by γ since it increases the pole of the error system (13) γ times.

Remark 2. For the bandwidth-based BESO, the bound of the estimation error is bandwidth-related but not monotonically related to the base bandwidth.

Remark 2 can be derived from (29); since $\boldsymbol{P}'$ and μ are not related to ω_o, the estimation error bound is actually determined by $\boldsymbol{h}'$. Furthermore, it can be seen from (30) that an increase in ω_o can reduce the impact of disturbances, but at the same time, it will amplify the impact of noise; thus, a higher ω_o does not necessarily guarantee a smaller L_3. This result reveals why it is difficult to obtain a small steady-state error and rapid transient performance with a constant bandwidth, such as in the LESO approach, when measurement noise exits.

Remark 3. For a bandwidth-based BESO with a given ω_o, a smaller γ always contributes more to reducing the impact of noise and improving the steady-state accuracy.

Remarks 1 to 3 reveal the role of the base bandwidth and DSO of the proposed BESO. A relatively high base bandwidth and DSO can guarantee a rapid transient process, while a smaller DSO can reduce the steady-state error. Consequently, the procedure for choosing the design parameters of the BESO can be fairly simple.

Step 1: η should be chosen to be as close to the lower bound as possible to achieve a better noise suppression ability.

Step 2: An appropriate ω_o can be obtained through a gradual incremental test from a relatively small initial value, and the steady-state error and transient performance will generally first decrease and then increase with an increase in ω_o. Thus, the recommended strategy is to choose the ω_o that achieves the best steady-state performance.

If the second step cannot provide a suitable ω_o that meets both the transient performance and noise suppression requirements, we can consider further reducing η to enhance its performance. Note that Corollary 1 is a sufficient condition, so the constraints on η can potentially be relaxed, but a sufficient test is required to ensure stability for the given system. We have reduced η to 0.21 to obtain better performance, and the BESO works stably in our test cases.

Remark 4. Although BESO has a switch mechanism, which makes it similar to the sliding mode observer (SMO) or the sliding mode disturbance observer (SMDO) [11,12,48], this similarity can easily be distinguished. First and foremost, the stability of BESO does not depend on the switching; i.e., whether it is working in low-bandwidth or high-bandwidth mode, BESO always converges, and the switching mechanism affects only its tracking and noise suppression performance. Second, the switch of BESO is based on the direction of the state estimation error, while the sliding surface of SMO is mostly a function of the estimation error and its integral. Finally, standard SMO approaches may be more sensitive to noise due to the switching mechanism.

3.2. BESO for a MIMO system

The BESO for the MIMO system in (1) can easily be obtained from that for the SISO system.

$$\begin{cases} \boldsymbol{e}_m = \hat{\boldsymbol{x}} - \boldsymbol{x}_m \\ \gamma_i = \eta_i^{-\text{sign}(\mathrm{d}|e_{m_i}|/\mathrm{d}t)} \\ \dot{\hat{\boldsymbol{x}}} = \boldsymbol{A}\boldsymbol{x}_m + \boldsymbol{B}\boldsymbol{u} + \hat{\boldsymbol{f}} + \boldsymbol{\beta}_{1_d}\boldsymbol{\gamma}_d\boldsymbol{e}_m \\ \dot{\hat{\boldsymbol{f}}} = \boldsymbol{\beta}_{2_d}\boldsymbol{\gamma}_d^2\boldsymbol{e}_m \end{cases}, \tag{43}$$

where $\boldsymbol{\beta}_{1_d} = \text{diag}(\boldsymbol{\beta}_1)$, $\boldsymbol{\beta}_{2_d} = \text{diag}(\boldsymbol{\beta}_2)$, and $\boldsymbol{\gamma}_d = \text{diag}(\boldsymbol{\gamma})$, and $\text{diag}(\cdot)$ returns a square diagonal matrix with the elements of the input vector on the main diagonal. $\boldsymbol{\beta}_1$ and $\boldsymbol{\beta}_2$ can also be chosen through the bandwidth approach as

$$\boldsymbol{\beta}_1 = 2\boldsymbol{\omega}_o, \boldsymbol{\beta}_2 = \boldsymbol{\omega}_o^2, \tag{44}$$

where $\boldsymbol{\omega}_o = [\omega_{o_1}, \omega_{o_2}, \ldots, \omega_{o_n}]^\top$ and ω_{o_i} represents the base bandwidth of the i^{th} channel of the BESO.

The estimation error dynamics can be derived as

$$\begin{cases} \dot{\boldsymbol{e}}_{\boldsymbol{x}} = \boldsymbol{\beta}_{1_d}\boldsymbol{\gamma}_d\boldsymbol{e}_{\boldsymbol{x}} + \boldsymbol{e}_{\boldsymbol{f}} + \boldsymbol{A}\boldsymbol{n}_{\boldsymbol{x}} - \boldsymbol{\beta}_{1_d}\boldsymbol{\gamma}_d\boldsymbol{n}_{\boldsymbol{x}} \\ \dot{\boldsymbol{e}}_{\boldsymbol{f}} = \boldsymbol{\beta}_{2_d}\boldsymbol{\gamma}_d^2\boldsymbol{e}_{\boldsymbol{x}} - \boldsymbol{\beta}_{2_d}\boldsymbol{\gamma}_d^2\boldsymbol{n}_{\boldsymbol{x}} - \boldsymbol{f}_a - \boldsymbol{f}_b \end{cases}. \tag{45}$$

Note that $\boldsymbol{\beta}_{1_d}$, $\boldsymbol{\beta}_{2_d}$ and $\boldsymbol{\gamma}_d$ are all diagonal. (45) can be decomposed into n decoupled second-order SISO systems as

$$\begin{bmatrix} \dot{e}_{x_i} \\ \dot{e}_{f_i} \end{bmatrix} = \begin{bmatrix} \beta_{1_i}\gamma_i & 1 \\ \beta_{2_i}\gamma_i^2 & 0 \end{bmatrix} \begin{bmatrix} e_{x_i} \\ e_{f_i} \end{bmatrix} - \begin{bmatrix} 0 \\ f_{a_i} + f_{b_i} \end{bmatrix} - \begin{bmatrix} \beta_{1_i}\gamma_i \\ \beta_{2_i}\gamma_i^2 \end{bmatrix} n_{x_i} + \begin{bmatrix} \boldsymbol{A}_i\boldsymbol{n}_{\boldsymbol{x}} \\ 0 \end{bmatrix}, \tag{46}$$

where $i = 1 \sim n$ and $\boldsymbol{A}_i$ is the i^{th} row of $\boldsymbol{A}$.

Consequently, the BESO for the MIMO system in (43) has exactly the same properties as that for the SISO system.

4. Comparisons between four promising ESOs

In this section, the BESO and three promising ESOs, namely, an LESO, an AESO, and an NHGESO, are compared in detail based on a first-order dynamic system. To investigate the insight mechanism of BESO, we choose a relative simple nonlinear one-dimensional model. Practical processes are usually high order and strongly correlated, so it is difficult to investigate which factor contributes to the performance alternation of ESOs. The SISO one-dimensional model we chose has no correlation between input and state, and the comparison work may be relatively simple. A more practical case is given in the next section to validate the feasibility of the BESO-based control method.

$$\begin{aligned} \dot{x} &= -5x + f(t) + u(t) \\ x_m &= x + n_x \end{aligned}, \tag{47}$$

where $x \in \mathbb{R}$ is measurable and has the initial state $x(0) = 0$, $u(t)$ is a constant input with amplitude 0.1, x_m is a noise-contaminated state, there is measurement noise, $n_x \sim N(0, 0.001)$, is a Gaussian white noise with variance 0.001, and $f(t)$ is a nonlinear disturbance w.r.t. t that has the following form:

$$\begin{aligned} f_a &= 0.1\sin(0.4t) + 0.2\sin(0.2t) \\ f_b &= \begin{cases} 0, & t < 6 \quad or \quad t \ge 13 \\ 1, & 6 \le t < 13 \end{cases} \\ f &= f_a + f_b, \end{aligned} \tag{48}$$

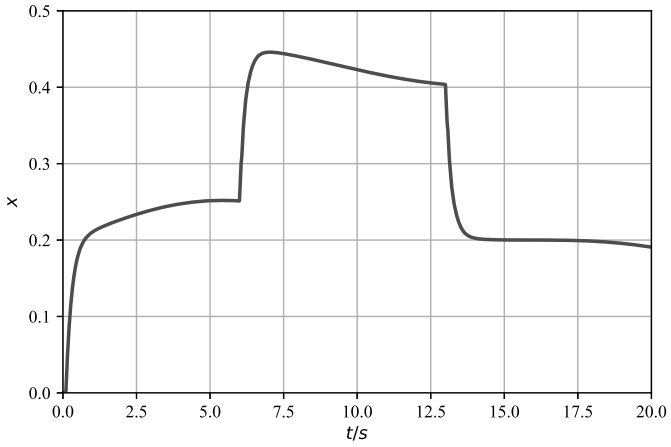

Fig. 1. Actual state.

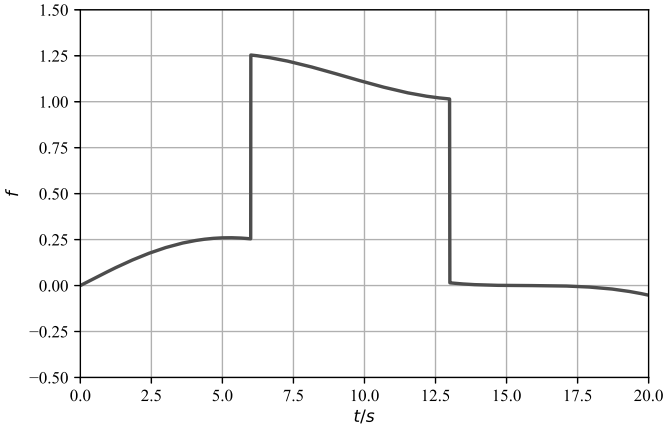

Fig. 2. Actual disturbance.

Table 1
Estimation performance indexes.

State estimation index J_{e_x}	$\frac{1}{t}\int_0^t \|\|x-\hat{x}\|\|_1 \mathrm{d}\tau$
Disturbance estimation index J_{e_f}	$\frac{1}{t}\int_0^t \|\|\boldsymbol{f}-\hat{\boldsymbol{f}}\|\|_1 \mathrm{d}\tau$

where f_a is a relatively small periodic disturbance and f_b is a larger abrupt disturbance. The trajectory and disturbances of the actual system are shown in Figs. 1 and 2.

To quantify the performances of the four ESOs, we introduce the performance indexes shown in Table 1.

4.1. Performance evaluation of ESOs

The evaluation is performed by optimizing the parameters of each ESO to obtain the best J_{e_x} and J_{e_f} for system (47) and then comparing the optimal results of each approach.

4.1.1. LESO

For the LESO, the adjustable parameter is the designed bandwidth [19], referred to as ω. As ω varies from 4 to 20 rad/s, the indexes are as listed in Table 2.

The best bandwidth in this scenario is 10 rad/s, which leads to the best J_{e_x} and the second smallest J_{e_f}. To show the detailed influences on the observation performance of the LESO due to bandwidth alternation, we choose 4, 10 and 20 rad/s as examples. The estimation errors for the state and disturbance with the above bandwidths are shown in Figs. 3 and 4.

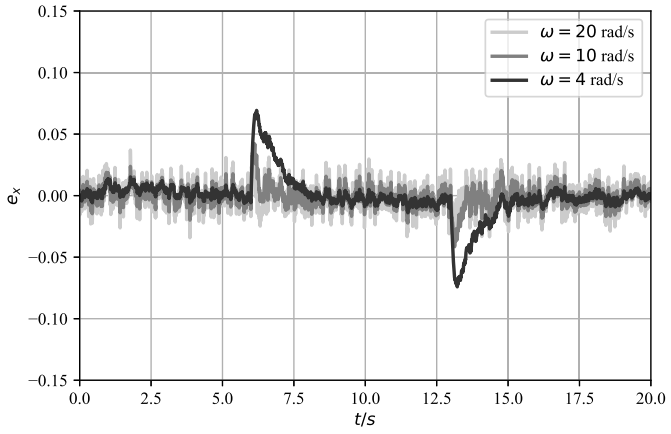

Fig. 3. State estimation errors of the LESO.

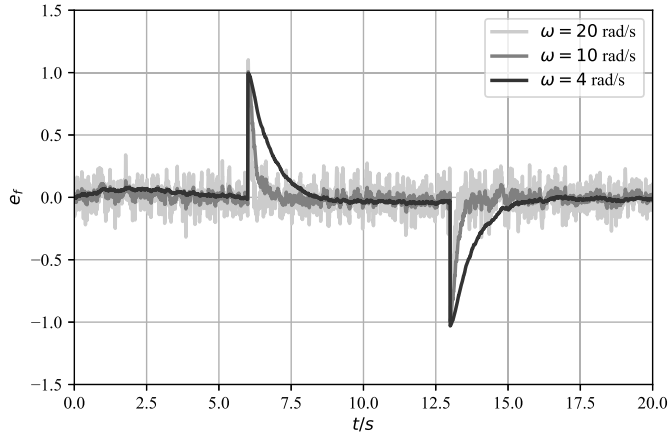

Fig. 4. Disturbance estimation errors of the LESO.

As shown in Figs. 3 and 4, the greater the bandwidth, the faster the transient processes that start at $t = 6$ s and $t = 13$ s are, and the more deteriorated the steady-state behaviors of the LESO are. This is the contradiction between the transient performance and noise attenuation in the LESO.

4.1.2. AESO

The gains of the AESO are calculated via formulas (64) and (54) in [42]. For a measurement noise variance of 0.001, it is straightforward that $\overline{R} = 0.001$ and $P_0 = \mathrm{diag}(0.001, 0.001)$. However, for $\overline{Q}$, it is relatively difficult to choose. Theoretically, $\overline{Q} = 1$ for the jump disturbance; however, choosing such a $\overline{Q}$ would result in unacceptably high gains, leading to an unstable observer. Otherwise, we ignore the jump feature of f and search for an appropriate $\overline{Q}$ in the range from 0.0005 to 0.032; the two indexes are listed in Table 3.

The best $\overline{Q}$ in this scenario is 0.004. We choose 0.0005, 0.004 and 0.032 as examples. The estimation errors for the state and disturbance with the corresponding gains are shown in Figs. 5 and 6.

The indexes show faint differences from the LESO case, but the AESO observations are smoother, which indicates its ability to cope with measurement noise. The reason the performance of AESO is not as good as that in [42] is that the disturbance $f(t)$ has a jump component in our simulation, while the case in [42] is smooth over the whole span. Therefore, $(f_i(t) - f(ih))(f_i(t) - f_i(ih))^\top \leq 0.004$ is violated in some instances, which may contribute to the perfor-

Table 2
Indexes of the LESO with a bandwidth varying from 4 to 20.

ω (rad/s)	4	6	8	10	12	14	16	18	20
J_{e_x}	0.008977	0.006394	0.005927	0.006095	0.006511	0.00697	0.00743	0.007876	0.008309
J_{e_f}	0.1012	0.06574	0.0541	0.05151	0.05391	0.0593	0.06677	0.07567	0.08564

Table 3
Indexes of the AESO as $\overline{Q}$ varies from 0.0005 to 0.032.

$\overline{Q}$	0.0005	0.001	0.002	0.004	0.008	0.016	0.032
J_{e_x}	0.01531	0.01030	0.007579	0.0063437	0.0061155	0.0063718	0.0070548
J_{e_f}	0.08334	0.059145	0.049347	0.050313	0.058732	0.075283	0.10336

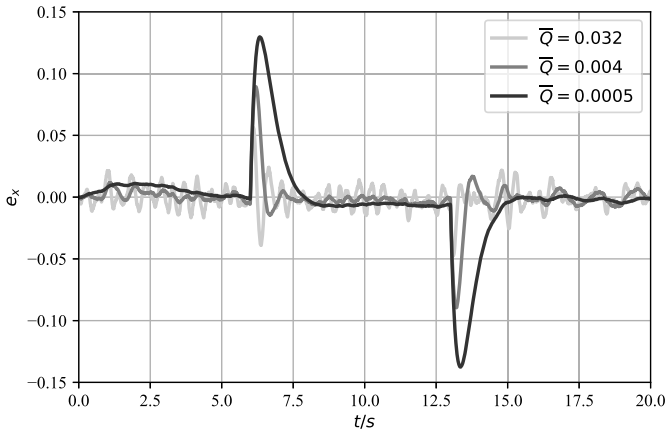

Fig. 5. State estimation errors of the AESO.

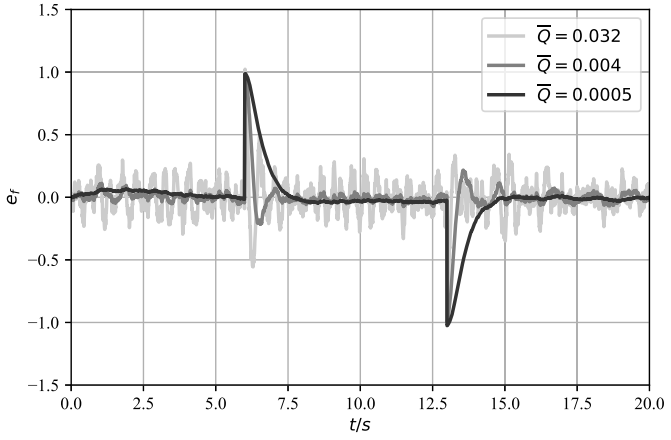

Fig. 6. Disturbance estimation errors of the AESO.

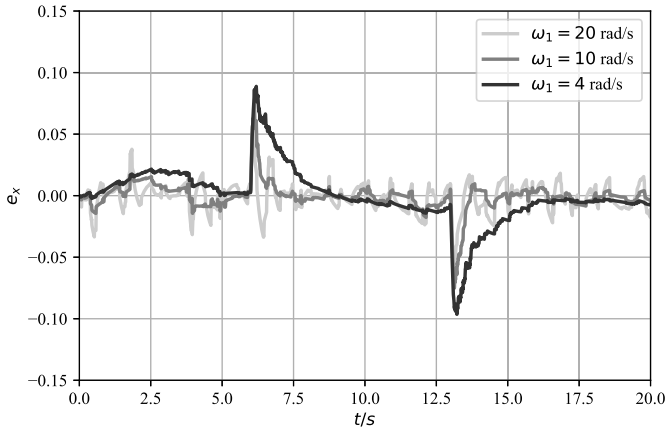

Fig. 7. State estimation errors of the NHGESO.

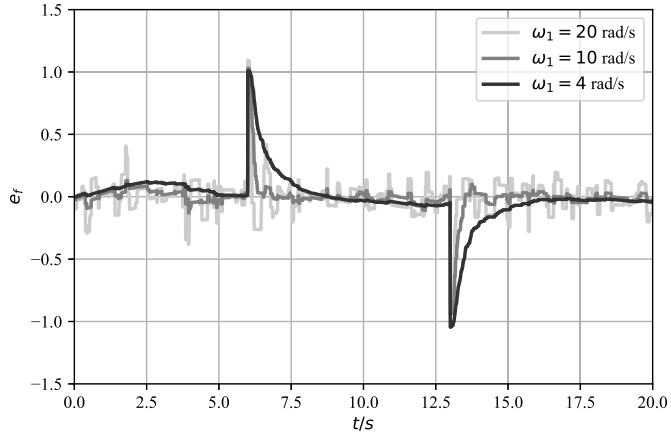

Fig. 8. Disturbance estimation errors of the NHGESO.

mance degradation. As $\overline{Q}$ grows, the overshoot immediately after the disturbance injection becomes high; otherwise, it lasts over a long period to converge to the actual trajectories. Therefore, choosing a suitable $\overline{Q}$ could be a challenge in the AESO for systems with abrupt and strong or rapidly varying disturbances.

4.1.3. NHGESO

For the above LESO and AESO, the gains are designed at the very beginning once and for all. However, according to the aforementioned cases, we already know that the observations deviate from the actual trajectories when abrupt disturbances are injected. If gains are leveled up in the injection instants, we can expect a faster transient process. However, observation errors are contributed primarily from measurement noise in the steady state; if the gains are switched to relatively small gains, the noise amplification by the high gains in the observations in the AESO and LESO scenarios can be attenuated. [44] used this strategy to cope with bounded measurement noise in state observers, and we extend their ideas to ESOs. We denote $\omega_1 = 1/\varepsilon_1$ and $\omega_2 = 1/\varepsilon_2$ and set $\omega_1 = 200\omega_2$. In [44], the ratio of ω_1 and ω_2 is greater than 1000; such a high ratio may cause extended state observer divergence because of the unbounded normally distributed measurement noise. The switching bound d is 0.06, and when ω_1 varies from 4 to 20, the two indexes are as listed in Table 4

Similar to the above two cases, we choose 4, 10 and 20 rad/s as examples. The estimation errors for the state and disturbance are shown in Figs. 7 and 8.

As shown in Figs. 7 and 8, the estimation results of the NHGESO are not as smooth as the results of the first two methods; they exhibit an obvious switch at the d-bound and show only a small

Table 4
Indexes of the NHGESO as the bandwidth ω_1 varies from 4 to 20.

ω_1 (rad/s)	4	6	8	10	12	14	16	18	20
J_{e_m}	0.01466	0.009059	0.006981	0.006323	0.00625	0.006604	0.007088	0.007646	0.008467
J_{e_f}	0.1038	0.06652	0.05227	0.04869	0.05112	0.05814	0.06782	0.07851	0.09151

Table 5
Indexes of the BESO with a base bandwidth varying from 4 to 20.

ω_o (rad/s)	4	6	8	10	12	14	16	18	20
J_{e_x}	0.005636	0.004666	0.004827	0.005179	0.005701	0.006174	0.006627	0.007054	0.007519
J_{e_f}	0.05975	0.04448	0.04277	0.0461	0.05422	0.06345	0.07406	0.08571	0.09943

Table 6
Performance indexes of the four ESOs.

–	BESO	LESO	AESO	NHGESO
J_{e_x}	0.004827	0.006095	0.006344	0.006323
$J_{e_x}/J_{e_x}^{*\,1}$	100.0%	126.3%	131.4%	131.0%
J_{e_f}	0.04277	0.05151	0.05031	0.04869
$J_{e_f}/J_{e_f}^{*\,2}$	100.0%	120.4%	117.6%	113.8%

[1,2] $J_{e_x}^*$ and $J_{e_f}^*$ represent the best values among the four ESOs.

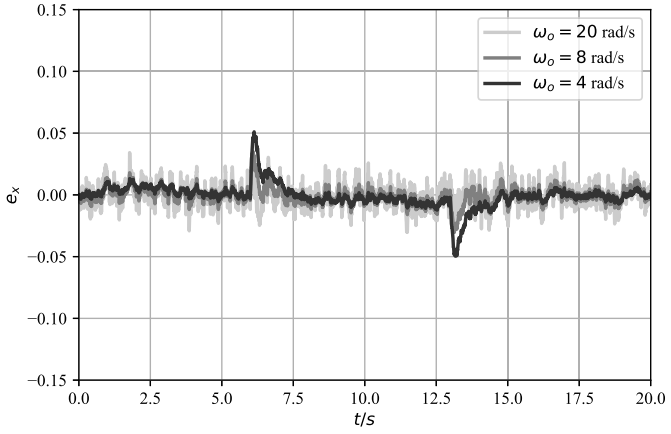

Fig. 9. State estimation errors of the BESO.

advantage over the LESO and AESO with the optimal parameters, which is contributed by the unbounded-measurement white noise, as will be illustrated in section 4.2.

4.1.4. BESO

The BESO has two adjustable parameters: the base bandwidth ω_o and the BSF η. We choose $\eta = 0.42$, which is very close to its lower bound. When ω_o varies from 4 to 20 rad/s, the two performance indexes are as listed in Table 5.

As shown in Table 5, as ω_o increases, J_{e_x} and J_{e_f} gradually decrease and then increase, reaching the optimal values at approximately 8 rad/s. The best indexes of the 4 ESOs are shown in Table 6, and the BESO is clearly superior among the four methods, showing improvements of more than 26% in J_{e_x} and 13% in J_{e_f}.

As usual, we choose the lowest, highest and optimal bandwidths as examples, and the estimation errors for the state and disturbance are given in Figs. 9 and 10.

As shown in Figs. 9 and 10, the responses are very smooth, similar to those of the LESO and AESO, indicating that the DSO has no visible impact on the estimation results. Notably, the BESO with $\omega_o = 4$ has a good noise attenuation capability, like the LESO and NHGESO, yet still has a faster transient process and a smaller peak error.

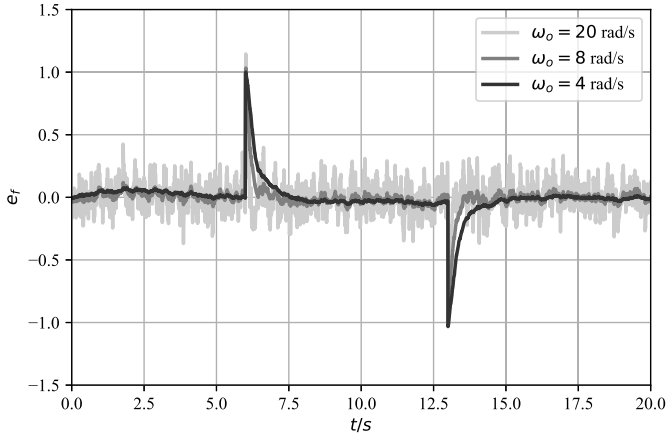

Fig. 10. Disturbance estimation errors of the BESO.

Table 7
Indexes in different time intervals.

Time Interval (s)		0–6	6–10	10–13	13–17	17–20
J_{e_x}	LESO	0.0052	0.0070	0.0053	0.0083	0.0045
	AESO	0.0029	0.0100	0.0034	0.0119	0.0039
	NHGESO	0.0063	0.0070	0.0050	0.0091	0.0031
	BESO	0.0040	0.0057	0.0049	0.0062	0.0033
J_{e_f}	LESO	0.029	0.0847	0.0293	0.0905	0.0228
	AESO	0.0239	0.0841	0.0223	0.0938	0.0282
	NHGESO	0.0378	0.0659	0.0312	0.0811	0.0218
	BESO	0.0264	0.068	0.0337	0.0657	0.0198

To analyze the performance of the transient and steady-state periods separately, we divide the whole simulation span into 5 intervals, where 0–6 s, 10–13 s and 17–20 s are the steady-state periods and 6–10 s and 13–17 s are the transient periods. For the case in which all four ESOs are configured with their optimal parameters, Table 7 gives the two indexes in different time intervals.

In the steady-state period, the AESO always has the best performance in both the state and disturbance channels, and BESO is the second best. In transient periods, the BESO always has the best estimation performance after a jump disturbance injection, and the AESO degrades significantly in these intervals. To evaluate the transient performance, the time needed for the four ESOs to converge into strips $e_x < 0.01$ and $e_f < 0.1$ is given in Table 8.

The transient times indicate that the BESO is far faster than the other methods. For a detailed discussion, the estimation results for the state and disturbance produced by the four ESOs with their optimal parameters are shown in Figs. 11 and 12.

According to the simulation results, three advantages of the BESO for systems with measurement noise are highlighted. First, the BESO has a faster transient process than that of the other three methods, yet it is implemented via a relatively low base bandwidth, which implies a preferred noise attenuation. Second,

Table 8
Transient time.

Jump time (s)	State t_s (s)		Disturbance t_s (s)	
	6	13	6	13
LESO	0.665	0.701	0.503	0.502
AESO	0.802	0.901	0.685	0.901
NHGESO	0.77	0.555	0.655	0.515
BESO	0.280	0.440	0.335	0.440

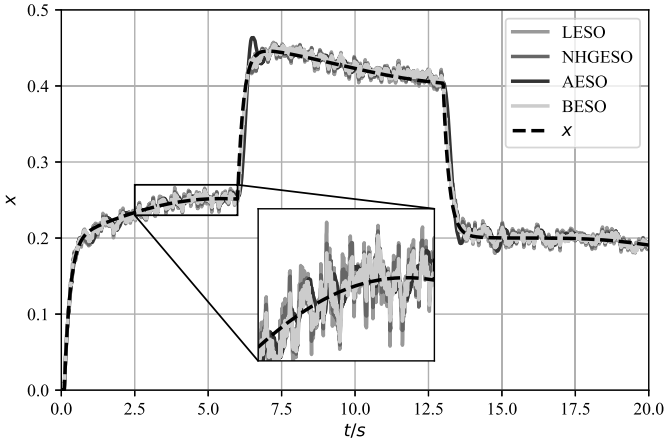

Fig. 11. State estimation with the four ESOs.

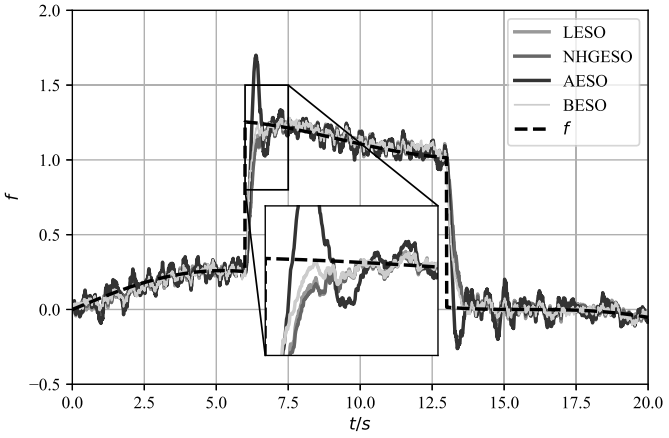

Fig. 12. Disturbance estimation with the four ESOs.

the BESO has no overshoot, even though the optimal switched high bandwidth ($\omega_o/\eta \approx 19$) is much greater than the equivalent bandwidth ($\sqrt{41.1595} \approx 6.5$) of the AESO's disturbance estimation channel. Finally, the two indexes of the BESO increase by at least 13%, which indicates its effectiveness. These results demonstrate that the BESO indeed alleviates the contradiction between a fast transient process and steady-state noise attenuation.

4.2. Robustness of the ESOs to disturbance and noise changes

In the above case, we discussed estimations of unaltered disturbances and noise, and the best parameters of the ESOs were designed or sought such that they were compatible with the given scenario. However, disturbances and measurement noise are usually not steady in physical systems; thus, a practical ESO should also be robust in non-nominal situations.

To study the impacts due to periodic disturbance frequency variations, we replace f_a in (48) with the following form and keep the other parameters consistent with the previous case.

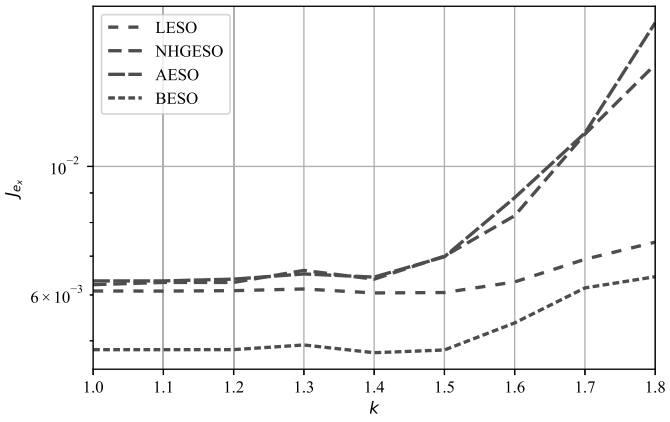

Fig. 13. J_{e_x} vs. frequency variation.

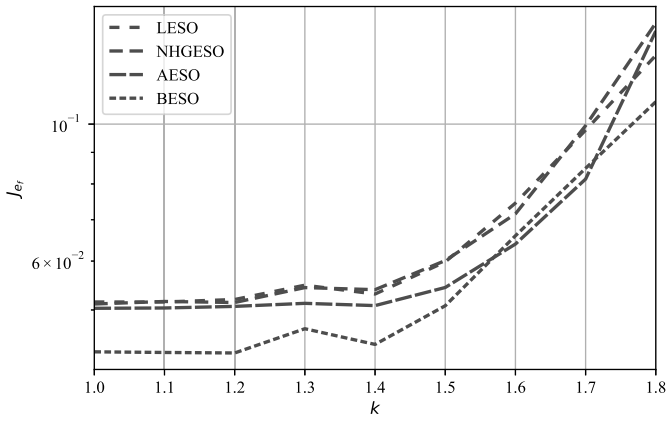

Fig. 14. J_{e_f} vs. frequency variation.

$$f_a = 0.1\sin(0.4kt) + 0.2\sin(0.2kt), \tag{49}$$

where k is the frequency multiplier. As k varies from 1 to 1.8, the two indexes of the four ESOs with the optimal parameters for $k = 1$ are shown in Figs. 13 and 14. A significant performance degradation of the AESO and NHGESO can be found for the state estimation error, while the curves of the BESO and LESO have similar trends, indicating that they are less affected by frequency changes.

Additionally, the four ESOs have different sensitivities to measurement noise. To quantify these sensitivities, we replace n_x with the following form, while the other parameters remain unchanged:

$$n_x \sim N(0, 0.001k). \tag{50}$$

As k varies from 1 to 1.8, the two indexes of the four ESOs with the optimal parameters for $k = 1$ are shown in Figs. 15 and 16.

As shown in these figures, the BESO always achieves relatively good performance among the four ESOs, which means it shows better robustness than the others to an unsteady frequency of the periodic disturbance and a varying noise power. Moreover, the AESO and NHGESO degrade quickly as the frequency of the periodic disturbance and noise power change because for the AESO and NHGESO, we need prior information. $\overline{Q}$ and a noise bound are needed to design the gains or switch bounds, but this prior information is usually unsteady. When these assumptions are violated by alternating conditions, the performance inevitably deteriorates.

5. A BESO-based closed-loop structurally damaged GTM control framework

The reason we want to improve the observation performance of ESOs is that we desire to obtain good closed-loop performance

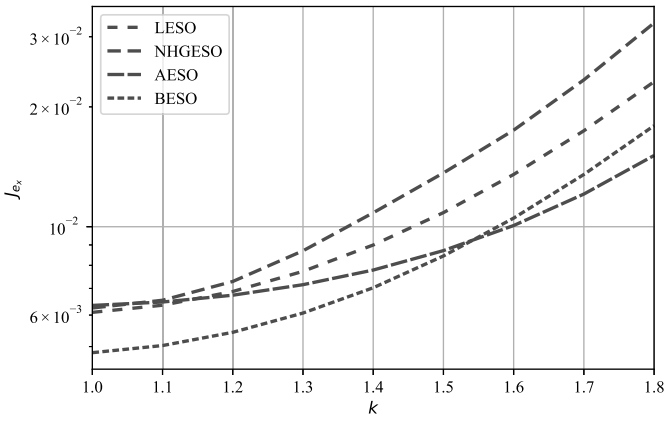

Fig. 15. J_{e_x} vs. noise variation.

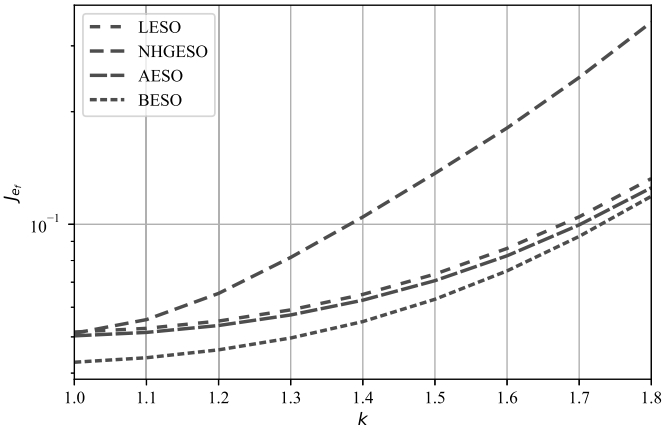

Fig. 16. J_{e_f} vs. noise variation.

using ESO-based approaches. As we have already demonstrated the efficiency and effectiveness of the BESO, we will use BESO-based disturbance rejection approach for a complex structurally damaged generic transport model (GTM) attitude control problem. The aim is to study whether the BESO still shows good performance for systems with high-order, coupling and strong disturbance.

The GTM was developed by NASA for the Intelligent Resilient Aircraft project of the Aviation Safety Program, and it has been widely used in research on structural damage control algorithms [49,50]. The steady operation point of a normal GTM is set as follows:

$$\begin{aligned}&\theta = 4.0962^\circ, \phi = 0^\circ, \psi = 0^\circ, p = 0^\circ/\text{s}, q = 0^\circ/s, r = 0^\circ/\text{s},\\ &V = 46.3\text{m/s}, \alpha = 4.0962^\circ, H = 304.8\text{m}, \beta = 0^\circ, X = 0\text{m},\\ &Y = 0\text{m}, \delta_e = 1.7721^\circ, \delta_a = 0^\circ, \delta_r = 0^\circ,\end{aligned} \tag{51}$$

where θ, ϕ and ψ are the pitch, roll and yaw angles, respectively; p, q and r denote the roll, pitch and yaw angular velocities, respectively; V is the airspeed; α is the angle of attack; β is the sideslip angle; H, X and Y represent the position of the aircraft; and δ_e, δ_a and δ_r are the deflections of the aileron, elevator and rudder, respectively. All the following state increments and control surface deflections have the same units as in (51).

The GTM can be formed as a linear time-varying model as expressed in (52) [50]:

$$\dot{\boldsymbol{x}} = \boldsymbol{A}(\mu)\boldsymbol{x} + \boldsymbol{B}(\mu)\boldsymbol{u} + \boldsymbol{H}(\mu)\boldsymbol{z} + \boldsymbol{d}(\mu), \tag{52}$$

where $\boldsymbol{x} = [\Delta\theta, \Delta\phi, \Delta\psi, \Delta q, \Delta p, \Delta r]^\top$ is the attitude-related state vector, $\boldsymbol{z} = [\Delta V, \Delta\alpha, \Delta H, \Delta\beta, \Delta X, \Delta Y]^\top$ is the position-related

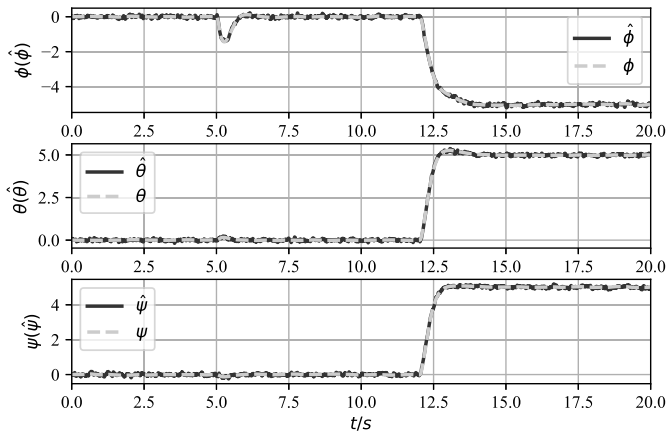

Fig. 17. State estimation.

vector, $\boldsymbol{u} = [\Delta\delta_e, \Delta\delta_a, \Delta\delta_r]^\top$ is the deflection of the control surfaces, $\mu \in [0, 100\%]$ is the percentage of wing damage, $\boldsymbol{d}$ is the unknown disturbance function of μ, which represents the large rotational torque caused by abrupt structural damage, namely, left wing tip loss in our simulation. Usually, $\boldsymbol{d}$ is a jump signal that is difficult to estimate on-line. Please refer to the Appendix for $\boldsymbol{d}$ of 20% wing damage.

When the left wing tip loses μ of its area, the damage model can transform into the nominal one with the lumped uncertainty $\boldsymbol{f}$, as expressed in (53):

$$\dot{\boldsymbol{x}} = \boldsymbol{A}(\mu_0)\boldsymbol{x} + \boldsymbol{B}(\mu_0)\boldsymbol{u} + \boldsymbol{f}, \tag{53}$$

where $\boldsymbol{f}$ is the combination of parameter uncertainty, external disturbance, state and input, as

$$\boldsymbol{f} = \Delta\boldsymbol{A}\boldsymbol{x} + \Delta\boldsymbol{B}\boldsymbol{u} + \boldsymbol{H}(\mu)\boldsymbol{z} + \boldsymbol{d}(\mu), \tag{54}$$

$\Delta\boldsymbol{A} = \boldsymbol{A}(\mu) - \boldsymbol{A}(\mu_0)$, $\Delta\boldsymbol{B} = \boldsymbol{B}(\mu) - \boldsymbol{B}(\mu_0)$, and $\mu_0 = 0$.

To achieve a desirable closed-loop performance, a reference model is given as

$$\dot{\boldsymbol{x}} = \boldsymbol{A}_{\boldsymbol{m}}\boldsymbol{x} + \boldsymbol{B}_{\boldsymbol{m}}\boldsymbol{r}, \tag{55}$$

in which

$$\boldsymbol{A}_{\boldsymbol{m}} = \begin{bmatrix} \boldsymbol{0} & \boldsymbol{I} \\ -\omega^2\boldsymbol{I} & -2\xi\omega\boldsymbol{I} \end{bmatrix}, \boldsymbol{B}_{\boldsymbol{m}} = \begin{bmatrix} \boldsymbol{0} \\ \omega^2\boldsymbol{I} \end{bmatrix}, \tag{56}$$

where $\omega = 5$ rad/s and $\xi = 0.7$ are selected for the desired dynamics.

Since $\boldsymbol{f}$ is unmeasurable, we can use the BESO in (43) to estimate $\boldsymbol{f}$ and substitute $\boldsymbol{f}$ with the estimate $\hat{\boldsymbol{f}}$; then, the control input has the following form:

$$\begin{aligned}\boldsymbol{u} = &-(\boldsymbol{B}(\mu_0)^\top\boldsymbol{B}(\mu_0))^{-1}\boldsymbol{B}(\mu_0)^\top\hat{\boldsymbol{f}} - \boldsymbol{K}^\top\boldsymbol{x}\\ &+(\boldsymbol{B}(\mu_0)^\top\boldsymbol{B}(\mu_0))^{-1}\boldsymbol{B}(\mu_0)^\top\boldsymbol{B}_{\boldsymbol{m}}\boldsymbol{r}.\end{aligned} \tag{57}$$

We also set $\eta = 0.42$ for stability. Through a linear search, we find that a BESO with base bandwidth $\omega_o = 24$ rad/s shows better performance than other BESOs. The variance of the noise is $\boldsymbol{\sigma}_{\boldsymbol{n_x}} = [0.01, 0.01, 0.01, 0.001, 0.005, 0.005]^\top$. The total simulation span is 20 s; the aircraft is undamaged in the time interval 0–5 s, the abrupt 20% left wing tip loss is injected at $t = 5$ s, and the incremental attitude command $\boldsymbol{r} = [-5^\circ, 5^\circ, 5^\circ]^\top$ is given at $t = 12$ s. The estimations of the states (channel ϕ, θ, ψ), lumped uncertainties (channel $\dot{\phi}, \dot{\theta}, \dot{\psi}$), tracking trajectories and control surface deflections are given in Figs. 17, 18, 19 and 20, respectively.

There is deviation in the roll channel, but no notable deviations exist in the pitch and yaw channels. Additionally, the deflections

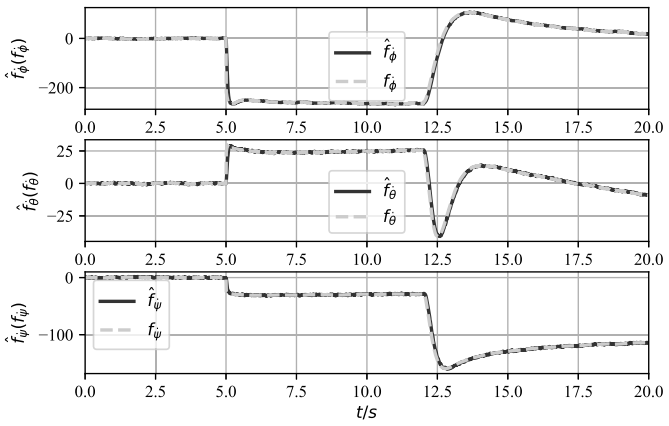

Fig. 18. Lumped uncertainty estimation.

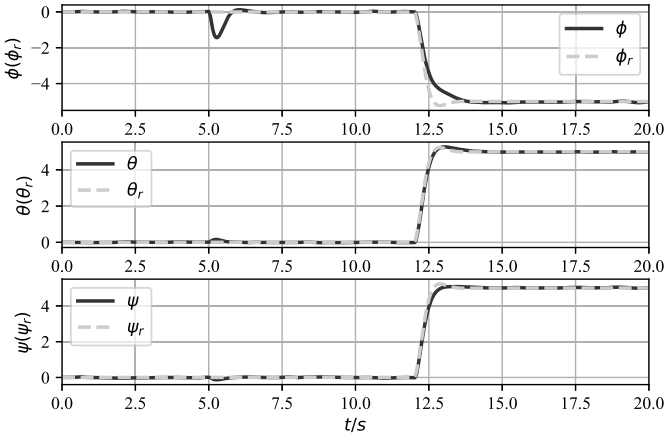

Fig. 19. State tracking.

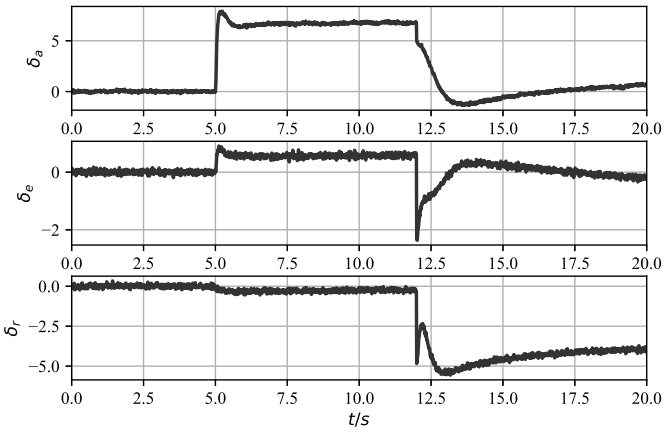

Fig. 20. Control surface deflection.

of the control surface are both less than 8°. The results show that the BESO-based approach has good tracking performance and noise attenuation capabilities, indicating the feasibility of the BESO for abruptly strongly disturbed systems.

6. Conclusion

In this paper, we propose a novel ESO approach that is easily implemented and has the so-called bi-bandwidth property. The proposed approach yields a significant performance improvement compared to existing methods and is less sensitive to drifts in the disturbance frequency and noise variance. The closed-loop control of the GTM demonstrates its validity for MIMO systems. Future work will focus on expanding the feasible range of the BSF, which may further improve the performance of the BESO.

Declaration of competing interest

The authors declare that they have no known competing financial interests or personal relationships that could have appeared to influence the work reported in this paper.

Acknowledgements

This research was funded by the National Natural Science Foundation of China (Grant Nos. 61273099 and 61304030).

Appendix A

The parameters of the GTM aircraft are as follows:

$$\boldsymbol{A}(\mu_0)=\begin{bmatrix}0&0&0&1&0&0\\0&0&0&0&1&0.0716\\0&0&0&0&0&1.0026\\0&0&0&-3.0362&0&0\\0&0&0&0&-4.6576&0.5481\\0&0&0&0&-0.3932&-1.0176\end{bmatrix} \tag{58}$$

$$\boldsymbol{B}(\mu_0)=\begin{bmatrix}0&0&0\\0&0&0\\0&0&0\\-43.2662&0&0\\0&39.5686&11.1409\\0&3.2818&-28.5370\end{bmatrix} \tag{59}$$

$$\boldsymbol{A}(20\%)=\begin{bmatrix}0&0&0&1&0&0\\0&0&0&0&1&0.0716\\0&0&0&0&0&1.0026\\0&0&0&-3.0217&-0.0613&0.0028\\0&0&0&-0.1264&-4.2841&0.5353\\0&0&0&-0.0134&-0.3640&-1.0222\end{bmatrix} \tag{60}$$

$$\boldsymbol{B}(20\%)=\begin{bmatrix}0&0&0\\0&0&0\\0&0&0\\-43.2900&1.2257&-0.0223\\0.3138&34.9176&11.2295\\0.0105&2.9083&-28.6308\end{bmatrix} \tag{61}$$

$$\boldsymbol{d}(20\%)=\begin{bmatrix}0&0&0&24.25&-219.15&-23.84\end{bmatrix}^\top \tag{62}$$

$$\boldsymbol{H}(20\%)= \tag{63}$$

$$\begin{bmatrix}0&0&0&0&0&0\\0&0&0&0&0&0\\0&0&0&0&0&0\\1.0466&-25.2807&-0.0030&-0.3201&0&0\\-9.4686&-43.4185&0.0270&-73.1188&0&0\\-1.0362&-5.9947&0.0029&25.1788&0&0\end{bmatrix}$$

$$\boldsymbol{K}=\begin{bmatrix}-0.5778&0&0\\0&0.6120&0.0704\\0&0.2389&-0.8486\\-0.0916&0&0\\0&0.0536&0.0199\\0&0.0706&-0.2015\end{bmatrix} \tag{64}$$

References

[1] L. Hou, H. Sun, Anti-disturbance attitude control of flexible spacecraft with quantized states, Aerosp. Sci. Technol. 99 (Apr.) (2020) 105760, https://doi.org/10.1016/j.ast.2020.105760.

[2] J. Zhang, J. Yan, L. Yang, Y. Mou, Robust IFNTSM-ESO control design for aircraft subject to parameter uncertainties, Int. J. Aeronaut. Space Sci. 21 (1) (2020) 239–250, https://doi.org/10.1007/s42405-019-00201-5.

[3] S. Yi, S. Xingling, Z. Wendong, Neural observer-based quantized output feedback control for MEMS gyroscope with guaranteed transient performance, Aerosp. Sci. Technol. (2020), https://doi.org/10.1016/j.ast.2020.106055.

[4] X. Yao, J.H. Park, L. Wu, L. Guo, Disturbance-observer-based composite hierarchical antidisturbance control for singular Markovian jump systems, IEEE Trans. Autom. Control 64 (7) (2018) 2875–2882, https://doi.org/10.1109/TAC.2018.2867607.

[5] A. Castillo, R. Sanz, P. Garcia, W. Qiu, H. Wang, C. Xu, Disturbance observer-based quadrotor attitude tracking control for aggressive maneuvers, Control Eng. Pract. 82 (2019) 14–23, https://doi.org/10.1016/j.conengprac.2018.09.016.

[6] S.J. Lee, S.H. Kim, H.J. Kim, Robust translational force control of multi-rotor uav for precise acceleration tracking, IEEE Trans. Autom. Sci. Eng. 17 (2) (2019) 562–573, https://doi.org/10.1109/TASE.2019.2935792.

[7] J. Chen, R. Sun, B. Zhu, Disturbance observer-based control for small nonlinear uav systems with transient performance constraint, Aerosp. Sci. Technol. 105 (2020) 106028, https://doi.org/10.1016/j.ast.2020.106028.

[8] J. Su, W. Chen, Further results on "reduced order disturbance observer for discrete-time linear systems", Automatica 93 (2018) 550–553, https://doi.org/10.1016/j.automatica.2018.04.032.

[9] D. Chwa, Robust nonlinear disturbance observer based adaptive guidance law against uncertainties in missile dynamics and target maneuver, IEEE Trans. Aerosp. Electron. Syst. 54 (4) (2018) 1739–1749, https://doi.org/10.1109/TAES.2018.2801392.

[10] M. Eom, D. Chwa, Robust swing-up and balancing control using a nonlinear disturbance observer for the pendubot system with dynamic friction, IEEE Trans. Robot. 31 (2) (2015) 331–343, https://doi.org/10.1109/TRO.2015.2402512.

[11] X. Wang, S. Sun, E.-J. van Kampen, Q. Chu, Quadrotor fault tolerant incremental sliding mode control driven by sliding mode disturbance observers, Aerosp. Sci. Technol. 87 (2019) 417–430, https://doi.org/10.1016/j.ast.2019.03.001.

[12] H. Rabiee, M. Ataei, M. Ekramian, Continuous nonsingular terminal sliding mode control based on adaptive sliding mode disturbance observer for uncertain nonlinear systems, Automatica 109 (2019) 108515, https://doi.org/10.1016/j.automatica.2019.108515.

[13] B. Marx, D. Ichalal, J. Ragot, D. Maquin, S. Mammar, Unknown input observer for LPV systems, Automatica 100 (2019) 67–74, https://doi.org/10.1016/j.automatica.2018.10.054.

[14] F. Xu, J. Tan, X. Wang, V. Puig, B. Liang, B. Yuan, Mixed active/passive robust fault detection and isolation using set-theoretic unknown input observers, IEEE Trans. Autom. Sci. Eng. 15 (2) (2017) 863–871, https://doi.org/10.1109/TASE.2017.2776998.

[15] W. Chen, J. Yang, L. Guo, S. Li, Disturbance-observer-based control and related methods—an overview, IEEE Trans. Ind. Electron. 63 (2) (2015) 1083–1095, https://doi.org/10.1109/TIE.2015.2478397.

[16] J. Han, From PID to active disturbance rejection control, IEEE Trans. Ind. Electron. 56 (3) (2009) 900–906, https://doi.org/10.1109/TIE.2008.2011621.

[17] B.Z. Guo, Z.L. Zhao, Active Disturbance Rejection Control for Nonlinear Systems: An Introduction, Wiley, Singapore, 2016.

[18] Q. Zheng, Z. Gao, Active disturbance rejection control: some recent experimental and industrial case studies, Control Theory Technol. 16 (4) (2018) 301–313, https://doi.org/10.1007/s11768-018-8142-x.

[19] Qing Zheng, L.Q. Gaol, Zhiqiang Gao, On stability analysis of active disturbance rejection control for nonlinear time-varying plants with unknown dynamics, in: 2007 46th IEEE Conference on Decision and Control, 2007, pp. 3501–3506.

[20] Z. Zhao, B. Guo, A novel extended state observer for output tracking of MIMO systems with mismatched uncertainty, IEEE Trans. Autom. Control 63 (1) (2018) 211–218, https://doi.org/10.1109/TAC.2017.2720419.

[21] Z. Zhao, B. Guo, A nonlinear extended state observer based on fractional power functions, Automatica 81 (2017) 286–296, https://doi.org/10.1016/j.automatica.2017.03.002.

[22] J. Zhang, X. Yang, L. Yang, Virtual-command-based model reference adaptive control for abrupt structurally damaged aircraft, Aerosp. Sci. Technol. 78 (2018) 452–460, https://doi.org/10.1016/j.ast.2018.04.043.

[23] H. Yang, L. Cheng, Y. Xia, Y. Yuan, Active disturbance rejection attitude control for a dual closed-loop quadrotor under gust wind, IEEE Trans. Control Syst. Technol. 26 (4) (2017) 1400–1405, https://doi.org/10.1109/TCST.2017.2710951.

[24] B. Li, Q. Hu, Y. Yang, Continuous finite-time extended state observer based fault tolerant control for attitude stabilization, Aerosp. Sci. Technol. 84 (2019) 204–213, https://doi.org/10.1016/j.ast.2018.10.006.

[25] K. Yan, M. Chen, Q. Wu, B. Jiang, Extended state observer-based sliding mode fault-tolerant control for unmanned autonomous helicopter with wind gusts, IET Control Theory Appl. 13 (10) (2019) 1500–1513, https://doi.org/10.1049/iet-cta.2018.5341.

[26] J. Liu, M. Sun, Z. Chen, Q. Sun, Output feedback control for aircraft at high angle of attack based upon fixed-time extended state observer, Aerosp. Sci. Technol. 95 (2019) 105468, https://doi.org/10.1016/j.ast.2019.105468.

[27] S. Wang, X. Ren, J. Na, T. Zeng, Extended-state-observer-based funnel control for nonlinear servomechanisms with prescribed tracking performance, IEEE Trans. Autom. Sci. Eng. 14 (1) (2016) 98–108, https://doi.org/10.1109/TASE.2016.2618010.

[28] M. Ramírez-Neria, H. Sira-Ramírez, R. Garrido-Moctezuma, A. Luviano-Juarez, Linear active disturbance rejection control of underactuated systems: the case of the Furuta pendulum, ISA Trans. 53 (4) (2014) 920–928, https://doi.org/10.1016/j.isatra.2013.09.023.

[29] Y. Li, B. Yang, T. Zheng, Y. Li, M. Cui, S. Peeta, Extended-state-observer-based double-loop integral sliding-mode control of electronic throttle valve, IEEE Trans. Intell. Transp. Syst. 16 (5) (2015) 2501–2510, https://doi.org/10.1109/TITS.2015.2410282.

[30] S. Hao, T. Liu, E. Rogers, Extended state observer based indirect-type ILC for single-input single-output batch processes with time- and batch-varying uncertainties, Automatica 112 (2020) 108673, https://doi.org/10.1016/j.automatica.2019.108673.

[31] H. Kwakernaak, R. Sivan, Linear Optimal Control Systems, Wiley-Interscience, New York, 1972.

[32] D. Cooper, A. Graham, Errors in state variable reconstruction when an observer is subject to constant input disturbances and measurement noise, IEEE Trans. Autom. Control 22 (1) (1977) 121–123, https://doi.org/10.1109/tac.1977.1101416.

[33] A.A. Prasov, H.K. Khalil, Tracking performance of a high-gain observer in the presence of measurement noise, Int. J. Adapt. Control Signal Process. 30 (8–10) (2016) 1228–1243, https://doi.org/10.1002/acs.2588.

[34] T. He, Z. Wu, Extended disturbance observer with measurement noise reduction for spacecraft attitude stabilization, IEEE Access 7 (2019) 66137–66147, https://doi.org/10.1109/ACCESS.2019.2918076.

[35] L. Wang, Z. Gao, X. Zhou, Z. Han, Exponential stabilization of a star-shaped thermoelastic network system based on the extended state observer with time-varying gains, IEEE Trans. Autom. Control (2020), https://doi.org/10.1109/TAC.2020.2976317.

[36] Z. Pu, R. Yuan, J. Yi, X. Tan, A class of adaptive extended state observers for nonlinear disturbed systems, IEEE Trans. Ind. Electron. 62 (9) (2015) 5858–5869, https://doi.org/10.1109/TIE.2015.2448060.

[37] J. Li, Y. Xia, X. Qi, Z. Gao, On the necessity, scheme, and basis of the linear–nonlinear switching in active disturbance rejection control, IEEE Trans. Ind. Electron. 64 (2) (2017) 1425–1435, https://doi.org/10.1109/TIE.2016.2611573.

[38] J. Han, Active Disturbance Rejection Control Technique-the Technique for Estimating and Compensating the Uncertainties (in Chinese), National Defense Industry Press, Beijing, 2009.

[39] Z. Dong, X. Huang, D. Li, Z. Zhang, Reactivity estimation based on an extended state observer of neutron kinetics, IEEE Trans. Nucl. Sci. 63 (5) (2016) 2691–2697, https://doi.org/10.1109/TNS.2016.2600648.

[40] T. Zhang, Z. Xu, C. Gerada, A nonlinear extended state observer for sensorless IPMSM drives with optimized gains, IEEE Trans. Ind. Appl. 56 (2) (2019) 1485–1494, https://doi.org/10.1109/TIA.2019.2959537.

[41] D. Won, W. Kim, D. Shin, C.C. Chung, High-gain disturbance observer-based backstepping control with output tracking error constraint for electro-hydraulic systems, IEEE Trans. Control Syst. Technol. 23 (2) (2014) 787–795, https://doi.org/10.1109/TCST.2014.2325895.

[42] W. Xue, W. Bai, S. Yang, K. Song, Y. Huang, H. Xie, Adrc with adaptive extended state observer and its application to air–fuel ratio control in gasoline engines, IEEE Trans. Ind. Electron. 62 (9) (2015) 5847–5857, https://doi.org/10.1109/TIE.2015.2435004.

[43] J.H. Ahrens, H.K. Khalil, High-gain observers in the presence of measurement noise: a switched-gain approach, Automatica 45 (4) (2009) 936–943, https://doi.org/10.1016/j.automatica.2008.11.012.

[44] A.A. Prasov, H.K. Khalil, A nonlinear high-gain observer for systems with measurement noise in a feedback control framework, IEEE Trans. Autom. Control 58 (3) (2012) 569–580, https://doi.org/10.1109/TAC.2012.2218063.

[45] Y. Cheng, Z. Chen, M. Sun, Q. Sun, Cascade active disturbance rejection control of a high-purity distillation column with measurement noise, Ind. Eng. Chem. Res. 57 (13) (2018) 4623–4631, https://doi.org/10.1021/acs.iecr.8b00231.

[46] H. Lin, P.J. Antsaklis, Stability and stabilizability of switched linear systems: a survey of recent results, IEEE Trans. Autom. Control 54 (2) (2009) 308–322, https://doi.org/10.1109/TAC.2008.2012009.

[47] R. Shorten, K.S. Narendra, O. Mason, A result on common quadratic Lyapunov functions, IEEE Trans. Autom. Control 48 (1) (2003) 110–113, https://doi.org/10.1109/TAC.2002.806661.

[48] Y. Deng, J. Wang, H. Li, J. Liu, D. Tian, Adaptive sliding mode current control with sliding mode disturbance observer for PMSM drives, ISA Trans. 88 (2019) 113–126, https://doi.org/10.1016/j.isatra.2018.11.039.

[49] J.A. Ouellette, Flight dynamics and maneuver loads on a commercial aircraft with discrete source damage, Ph.D. thesis, Virginia Polytechnic Institute and State University, 2010.

[50] J. Zhang, X. Xu, L. Yang, X. Yang, LPV model-based multivariable indirect adaptive control of damaged asymmetric aircraft, J. Aerosp. Eng. 32 (6) (2019) 04019095, https://doi.org/10.1061/(ASCE)AS.1943-5525.0001089.